Journal of Materials Chemistry C

ROYAL SOCIETY OF CHEMISTRY

PAPER

View Article Online
View Journal | View Issue

Cite this: J. Mater. Chem. C, 2025, 13, 13272

Carbon nanotube-regulated growth of metal–organic framework nanosheets for enhanced electrochemical energy storage†

Weibiao Guo,[a] Zhikuan Wang,[a] Yu Liang,[a] Shujun Liu,[b] Xuejun Xu,[a] Huixia Chao,[c] Chongxiong Duan *[a] and Hongxia Xi *[b]

Received 4th March 2025,
Accepted 19th May 2025

DOI: 10.1039/d5tc00963d

rsc.li/materials-c

The design and synthesis of innovative two-dimensional (2D) metal–organic framework (MOF) nanosheets with superior electrochemical performance have substantial impacts on energy storage. Herein, a series of Ni-Tdc/CNT composites with excellent electrical conductivity and mechanical properties was synthesized using 2D Ni-MOFs and CNTs *via* a simple one-step hydrothermal process in a DMF/H_2O mixed solvent. The incorporation of CNTs mitigated the stacking phenomenon of Ni-Tdc nanosheets, facilitated the transmission of electrons within the electrode and reduced the volume deformation of the electrode material during electrochemical reactions. The unique, large-sized nanosheet structure of the Ni-Tdc/CNT composites increased accessible redox-active sites while promoting the penetration of electrolyte ions. The optimal Ni-Tdc/CNTs-20 composite (with a CNT mass fraction of 8%) obtained by modulating the mass fraction of CNT demonstrated a high specific capacity of 373.1 C g^{-1} (757.8 F g^{-1}) at a current density of 1 A g^{-1} and an excellent rate capacity of 79.4% retention at 10 A g^{-1}. Moreover, an asymmetric supercapacitor device composed of Ni-Tdc/CNTs-20 composite and active carbon exhibited a high energy density of 45 W h kg^{-1} at a power density of 8000 W kg^{-1} and an outstanding cycle life with a capacitance retention of 74.1% after 5000 cycles. This work demonstrates the enormous potential for energy storage and conversion applications by integrating 2D Ni-MOF and CNT composites.

1. Introduction

Swift economic development has instigated multifaceted energy and environmental challenges encompassing the dwindling supply of traditional fossil fuels and excessive emission of carbon dioxide and other gaseous industrial emissions. Hence, green and clean sources of energy are high in demand.[1] With the increasing demand for electric vehicles and electronics, the development of high-performance energy storage devices is imminent.[2] Supercapacitors have been highly regarded as promising energy storage solutions owing to their exceptional power density, swift charging–discharging rates, and impressive longevity, ensuring prolonged usage cycles.[3,4] These devices not only compensate for the low power density of batteries but also provide solution to the low energy density of capacitors. Currently, research efforts aimed at enhancing the electrochemical performance of supercapacitors are primarily focused on improving their energy density while maintaining their inherent advantages. The primary structure of supercapacitors comprises cathode and anode materials, current collectors, electrolyte solutions, and separators, with the electrode materials being the crucial factor influencing their electrochemical performance.[5] A diverse array of electrode materials, including carbonaceous materials, conductive polymers, and transition metal oxides, has been extensively researched and developed in recent years.[6–9] Supercapacitors have significantly better power density than battery-based systems, but their energy density is at a disadvantage; thus, improving the energy density and achieving better charge storage capabilities are the main focus of the current research.[10] From a chemical perspective, battery-type electrode materials possess rich redox-active centers, making them capable of delivering substantial energy storage capacity and energy density. The newly developed electrode materials and devices, while retaining the traditional merits of supercapacitors, increasingly favor the incorporation of the

[a] School of Materials Science and Engineering, Foshan University, Foshan, 528231, China. E-mail: cechxduan@fosu.edu.cn
[b] School of Chemistry and Chemical Engineering, South China University of Technology, Guangzhou, 510640, China. E-mail: cehxxi@scut.edu.cn
[c] Guangxi Key Laboratory of Green Chemical Materials and Safety Technology, Guangxi Engineering Research Center for New Chemical Materials and Safety Technology, College of Petroleum and Chemical Engineering, Beibu Gulf University, Qinzhou, 535011, China

† Electronic supplementary information (ESI) available. See DOI: https://doi.org/10.1039/d5tc00963d

high-capacity advantage associated with battery-type energy storage devices. Consequently, battery-type electrode materials have emerged as a pivotal research focus within the realm of energy storage.

Metal–organic frameworks (MOFs), characterized by abundant metallic active centers, exhibit excellent properties that mirror those of battery-type materials, prompting intense interest and scrutiny from researchers active in the realm of energy storage.[11] However, the relatively low electrical conductivity and suboptimal stability of MOFs continue to hinder their widespread adoption as electrode materials.[12] Furthermore, because of the sluggish ion diffusion kinetics during electrochemical reactions,[13] the charge–discharge efficiency also requires improvement. Therefore, many methods, such as composite strategies,[14] surface modification,[15] and atomic doping,[16] have been explored and employed to manipulate the structure and functionality of MOFs to enhance their performance and applicability. Studies have demonstrated that the use of composite strategies, which involve integrating MOFs with other functional materials, can effectively harness the unique properties of these functional materials (such as excellent electrical conductivity and superior mechanical properties) while preserving the advantages of MOF porous channels and active sites to achieve multifunctionality in terms of both physical and chemical properties.[17–19]

The conductivity and cycling stability of materials with stable structures, combined with MOFs as electrode materials, were greatly enhanced. Such as compositing with carbon-based materials harnesses synergies, resulting in superior capacitive performance. Liu *et al.*[20] used an ultrasonic approach to fabricate NiCo-MOF/acetylene black. The introduced acetylene black was consistently diffused throughout NiCo-MOF nanosheets, establishing a conductive network while preventing excessive aggregation of the nanosheets. Compared with pristine NiCo-MOFs, the NiCo-MOF/acetylene black composite electrode exhibited a higher specific capacitance of 916.1 F g^{-1}. This unique structure facilitated access to more redox-active surfaces and shortened electron transfer and ion diffusion distances, thereby significantly enhancing the electrode's specific capacitance. Among the carbon-based materials used in MOF composites, CNTs have garnered significant attention due to their unique one-dimensional structure. Based on the favourable electrical conductivity and excellent mechanical properties,[21] CNTs can fully compensate for the insufficient conductivity and stability of MOFs. Zhang *et al.*[22] successfully synthesized CNTs@Mn-MOF by incorporating carboxylated CNTs into the precursor solution of Mn-MOFs. The added CNTs provided stable mechanical support and a conductive network for the MOF composites, resulting in an increase in the specific capacity of the composite electrode from 43.2 F g^{-1} for pristine Mn-MOF to 203.1 F g^{-1}. Furthermore, after undergoing 3000 repeated charge–discharge cycles, the CNTs@Mn-MOF electrode material exhibited an initial capacity retention rate of 88%, demonstrating its exceptional stability. Shoeb *et al.*[23] indicated that the $SmVO_4$–MoS_2–CNT nanocomposite with CNT (Sm–Mo–C5) exhibited high electrical conductivity, efficient ion diffusion, and maximum electrochemical performance. The Sm–Mo–C5 nanocomposite benefits from the enhanced conductivity and mechanical strength of CNT, the stability and redox activity of $SmVO_4$, and the large specific surface area and redox sites of MoS_2. These components work together to enhance the electrochemical performance. The SSD prepared by VARTM has a specific capacitance of 0.287 F cm^{-2} at a current density of 2 A cm^{-2}, retains 72.5% of its initial capacitance after 50 000 charge–discharge cycles, and reaches a maximum energy density of 79.86 W h kg^{-1} at a power density of 1017.69 W kg^{-1}. Lu *et al.*[24] fabricated a composite material (Ni-MOF/C-CNTs) consisting of interpenetrating carboxylated carbon nanotubes (C-CNTs) and MOFs. By incorporating an appropriate amount of C-CNTs during the synthesis of MOFs, the morphology and thickness of the MOF nanosheets can be effectively regulated. The oxygen-containing functional groups on the surface of the functionalized C-CNTs provide sites for adsorbing metal ions, which effectively reduces the degree of stacking of MOF nanosheets as they gradually nucleate and grow. The as-synthesized Ni-MOF/C-CNTs-40 not only possesses fast electron transport channels that compensate for the relatively low conductivity of MOF nanosheets but also exposes a large number of redox-active sites that promote electrochemical reactions, significantly enhancing its capacity performance. The as-synthesized Ni-MOF/C-CNTs-40 electrode exhibited excellent specific capacitance (680 C g^{-1} at 1 A g^{-1}) and good capacity retention (442 C g^{-1} at 10 A g^{-1}). The hybrid supercapacitor assembled from this electrode achieved a high energy density of 44.4 W h kg^{-1} at a power density of 440 W kg^{-1}. Previous research has emphasized the significance of investigating supercapacitor electrodes under low-mass loadings (typically ranging from 1.2 to 2.8 mg cm^{-2}). This approach not only enhanced the understanding of fundamental electrochemical processes, such as specific capacitance, ion transport, and electrode stability but also provided valuable insights for optimizing electrode materials and configurations. These insights are crucial for addressing the challenges encountered during the transition to higher mass loadings, such as increased resistance and extended ion transport pathways. Knowledge derived from low-mass-loading studies can guide the design of high-mass-loading electrodes, thereby contributing to the mitigation of issues such as poor electrolyte penetration and sluggish ion kinetics. Therefore, the rational design and construction of MOFs and CNTs as electrodes for supercapacitors are highly desirable approaches to enhancing energy density.

Herein, CNTs and Ni-MOF were combined through a solvothermal method to create Ni-Tdc/CNT composites, which inherited the beneficial properties of both materials. These composites featured a continuous 2D structure that offered ample open space for electrolyte-ion diffusion, alongside axial channels dominated by CNTs that efficiently conducted electrons. The large number of exposed, accessible active sites is also conducive to the promotion of redox kinetics and the enhancement of electrochemical reaction efficiency. The introduction of CNTs also effectively mitigates the volume expansion effect of the nanosheet structure during the charging and discharging process and enhances the stability of the composite.

The experimental results indicated that the optimal Ni-Tdc/CNTs-20 (CNTs mass fraction of 8%) obtained by modulating the CNT mass fraction demonstrates a high specific capacity of 373.1 C g^{-1} (757.8 F g^{-1}) at the current density of 1 A g^{-1} and a better rate capacity (79.4% retention at 10 A g^{-1}). Moreover, an asymmetric supercapacitor device composed of Ni-Tdc/CNTs-20 and active carbon exhibited a high energy density of 45 W h kg^{-1} at a power density of 8000 W kg^{-1} and an outstanding cycle life with a capacitance retention of 74.1% after 5000 cycles.

2. Experimental

2.1. Materials

All chemicals were commercially available and used without further purification, including Ni $(NO_3)_2{\cdot}6H_2O$ (98%, Guangzhou Chemical Reagent), 2,5-thiophenedicarboxylic acid (H_2Tdc, 98%, Aladdin Reagent), *N,N*-dimethylformamide (DMF, Tianjin Damao Reagent), absolute ethanol (Tianjin Damao Reagent), *N*-methyl-2-pyrrolidone (NMP, Tianjin Damao Reagent), Polyvinylidene fluoride (PVDF, Zhengzhou Jinghong New Energy Technology CO), KOH (85%, Tianjin Damao Reagent), hydrochloric acid (HCl, Guangzhou Chemical Reagent), and active carbon (AC, Shenzhen Kejing Star Technology Co. Ltd). All aqueous solutions were prepared using high-purity deionized water (DI-water, resistance 18 MΩ cm^{-1}).

2.2. Synthesis of the Ni-Tdc and Ni-Tdc/CNT composites

The synthesis of Ni-Tdc involved dissolving 0.5 mmol of H_2Tdc (88 mg) in 25 mL of DMF with stirring for 5 min to form solution A. Subsequently, 0.5 mmol of Ni $(NO_3)_2{\cdot}6H_2O$ (148 mg) was dissolved in 5 mL of deionized water and added dropwise to solution A. The mixture was then transferred to a 50 mL high-pressure reactor and heated at 120 °C for 3 h. After cooling, the product was filtered, washed with deionized water and ethanol (three times each), and dried in a vacuum oven at 80 °C for 12 h, resulting in a light green powdery Ni-Tdc material.

The synthesis of Ni-Tdc/CNT composites was conducted *via* a solvothermal method. Initially, 0.5 mmol of H_2Tdc was weighed and dissolved in 25 mL of DMF with stirring for approximately 5 min to form solution B. Subsequently, a predetermined amount of CNTs was added, and the mixture was sonicated for 30 min. Subsequently, 0.5 mmol of Ni $(NO_3)_2{\cdot}6H_2O$ was dissolved in 5 mL of deionized water to form solution C. Solution C was added dropwise to solution B using a dropper, and sonication was continued for 1 h. The homogeneous dispersion was then transferred to a 50 mL high-pressure reactor liner and subjected to thermal treatment at 120 °C for 12 h in a constant-temperature oven. Upon completion and cooling to room temperature, the product was isolated *via* vacuum filtration, thoroughly rinsed with deionized water and ethanol (three times each), and dried under vacuum at 80 °C for 12 h to yield the powdered Ni-Tdc/CNTs composite. CNTs were introduced at varying masses of 10 mg, 20 mg, 30 mg, and 40 mg, resulting in composites designated as Ni-Tdc/CNTs-10, Ni-Tdc/CNTs-20, Ni-Tdc/CNTs-30, and Ni-Tdc/CNTs-40, respectively. Additionally, Ni-Tdc was synthesized under identical conditions, except in the absence of CNTs.

2.3. Synthesis of the Ni-Tdc and Ni-Tdc/CNTs working electrode

Both the Ni-Tdc working electrode and the Ni-Tdc/CNTs working electrodes were prepared using a coating method with a 1 cm × 2 cm nickel foam serving as the current collector. The nickel foam was ultrasonically cleaned with hydrochloric acid, deionized water, and ethanol for 15 min each and then dried for use. The specific steps for preparing the working electrode are as follows: initially, the active materials (Ni-Tdc, Ni-Tdc/CNTs-10, Ni-Tdc/CNTs-20, Ni-Tdc/CNTs-30, and Ni-Tdc/CNTs-40), conductive carbon black, and PVDF were mixed in a mass ratio of 8 : 1 : 1 in an agate mortar and thoroughly ground to ensure homogeneous mixing. In addition, an appropriate amount of NMP was added dropwise to the ground powder mixture, and the mixture was stirred with a glass rod until a uniform paste mixture was formed. Furthermore, the paste was coated onto the surface of the pretreated NF current collector and then placed in a vacuum oven to dry at 80 °C for 12 h. After removal, the mass of the electrode was measured, and the mass of the active material on the coated electrode was calculated using the gravimetric method.

2.4. Characterizations

The morphologies and microstructures of the electrode materials were investigated using X-ray diffraction (XRD) patterns (Bruker D8 Advanced X-ray diffractometer, CuKα radiation: λ = 0.15406 nm), Fourier transform infrared (FTIR) spectra (Vector 33, Bruker, Germany), Raman spectra (alpha300R, WITec, Germany), scanning electron microscopy (SEM, SC8820, Japan), and high-resolution transmission electron microscopy (HRTEM, JEM-2100). The chemical compositions and oxidization states of the samples were analyzed by X-ray photoelectron spectroscopy (XPS) using a Thermo ESCALAB 250Xi X-ray photoelectron spectrometer. The conductivity of the samples was analyzed using a resistivity tester (ST2643).

2.5. Electrochemical measurements

The electrochemical performance of the obtained electrodes was assessed by cyclic voltammetry (CV), galvanostatic charge–discharge (GCD) and electrochemical impedance spectroscopy (EIS) measurements on a CS2350H workstation. For the three-electrode configuration, prepared electrodes (10 × 10 mm^2) were used directly as the working electrodes. Platinum and Hg/HgO were used as the counter and reference electrodes, respectively. The electrolyte used in the experiments was a 1 M KOH solution at room temperature.

The specific capacitance (C_s, F g^{-1}) and specific capacity (C_m, C g^{-1}) of all the materials tested were derived from the GCD curves according to eqn (1) and (2)

$$C_s = (I \times \Delta t)/(m \times \Delta V) \quad (1)$$

$$C_m = (I \times \Delta t)/m \quad (2)$$

where I (mA) denotes the current in the GCD tests, m (mg) represents the mass loading of the active materials, Δt (s) is the discharge time, and ΔV (V, excluding the IR drop) denotes the discharge voltage range.

The capacitance contribution ratio was calculated using eqn (3) to determine the b value:

$$I = av^b \quad (3)$$

where I is the current density (mA cm^{-2}), v is the scan rate (mV s^{-1}), and a and b are fitted constants.

The k values at different scan rates were calculated using eqn (4) to assess the capacitive control of the electrode:

$$I(v) = k_1v + k_2v^{1/2} \quad (4)$$

where k_1v and $k_2v^{1/2}$ correspond to the surface double-layer capacitance (EDLs) and pseudocapacitive/diffusion capacitance behaviors, respectively.

In a two-electrode configuration, the electrochemical measurements of the asymmetric supercapacitor cells were carried out with the Ni-Tdc/CNTs-20 as the positive electrode and active carbon (AC) as the negative electrode. The negative electrode was prepared by stirring and mixing AC, acetylene black, and PVDF at an 8 : 1 : 1 weight ratio in NMP. The resulting slurry was uniformly coated onto the surface of an NF substrate with dimensions of 10 × 10 mm^2, followed by drying at 80 °C for 12 h. Asymmetric supercapacitor device positive and negative mass matching eqn (5):

$$m^+/m^- = (C^- \times \Delta E^-)/(C^+ \times \Delta E^+) \quad (5)$$

where C^+ and C^- (F g^{-1}) represent the mass-specific capacitance of the positive and negative electrodes, respectively, ΔE^+ and ΔE^- (V) are the potential windows of the positive and negative electrodes, respectively, and m^+ and m^- correspond to the active material loading of the positive and negative electrodes, respectively.

The energy density (E, W h kg^{-1}) and power density (P, W kg^{-1}) of the asymmetric supercapacitor were calculated using eqn (6) and (7) as follows:

$$E = (C \times \Delta V^2)/(2 \times 3.6) \quad (6)$$

$$P = 3600E/\Delta t \quad (7)$$

where E (W h kg^{-1}) and P (W kg^{-1}) represent the device energy density and power density, respectively, C (F g^{-1}) is the mass-specific capacitance of the device, and ΔV (V) and Δt (s) represent the operating voltage window and discharge time, respectively.

2.6. Theoretical calculation

All calculations were conducted based on the first principles of density functional theory (DFT) calculations by using the Vienna Ab-initio Simulation package. The projector-augmented-wave (PAW) method and Perdew–Burke–Ernzerhof (PBE) function were used to describe the exchange–correlation interaction. All calculations were performed using an energy cutoff of 450 eV. Monkhorst–Pack k-point was set to be 1 × 3 × 2 for geometry optimization. The electronic energy and forces converged to within 10^{-5} eV atom^{-1} and 0.01 eV Å^{-1}, respectively.

3. Results and discussion

3.1. Structural characterization

The synthesis process of Ni-Tdc/CNT composites is illustrated in Scheme 1 using a simple solvothermal method. As shown in Fig. 1(a), the crystalline structure of the Ni-Tdc/CNT composites was thoroughly examined by XRD analysis. A comparative assessment of the XRD spectra of Ni-Tdc/CNT composites with various CNT concentrations relative to pristine Ni-Tdc revealed no changes in the Ni-Tdc crystal structure upon CNT incorporation. The Bragg diffraction peaks at 9.4°, 15°, and 18.7° in the XRD spectra correspond to the (020), (110), and (040) crystalline planes of Ni-Tdc, respectively.[25] Notably, all Ni-Tdc/CNT composites exhibited the same crystal structure as pristine Ni-Tdc. However, the peak intensities at these positions were reduced in the composites, which is attributed to the introduction of CNTs. In addition, a diffraction peak at 26° was observed in the Ni-Tdc/CNT composites, corresponding to the (002) crystal plane of graphitized carbon.[26] This peak intensity increased with the incorporation of more CNTs. This analysis confirmed the successful incorporation of CNTs into Ni-Tdc, resulting in composite formation without altering the underlying Ni-Tdc structure.

FTIR spectroscopy was used to characterize the functional group information of the MOF/CNT composites and the pristine Ni-Tdc sample. As shown in Fig. 1(b), all samples exhibit pronounced absorption peaks at 1572 cm^{-1} and 1365 cm^{-1}, which correspond to the asymmetric and symmetric stretching vibrations, respectively, of the H_2Tdc ligand (–COO–) within the MOFs.[27] The stretching vibration of –OH was identified at the absorption peak at 3605 cm^{-1}, indicating that H_2O molecules were involved in the coordination within the structure of lamellar MOFs. Four characteristic peaks, located at 1131, 1028, 815 and 709 cm^{-1}, were attributed to the C–H stretching vibration in the thiophene ring,[28] which is characteristic of the thiophene ligand. The characteristic absorption peak spectra of Ni-Tdc/CNT composites remained similar after the introduction of the CNTs, indicating that the samples retained their original structure. Furthermore, it is observable that the intensity of the absorption peaks decreases with the increasing addition of CNTs.

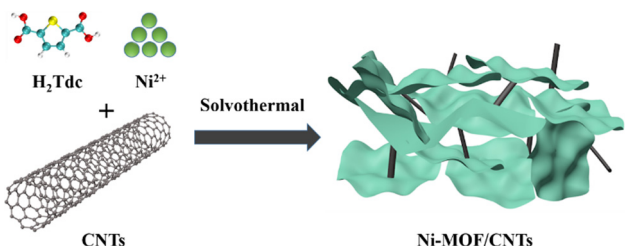

Scheme 1 Schematic for the synthesis of Ni-Tdc/CNT composites.

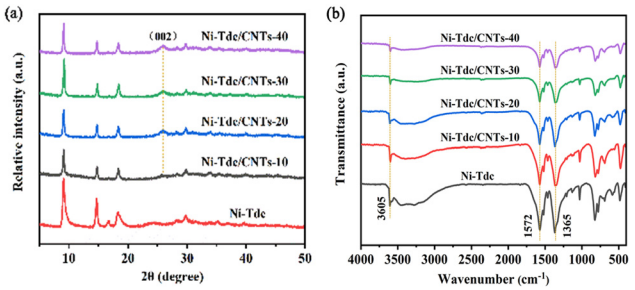

Fig. 1 (a) XRD patterns and (b) FTIR spectra of different Ni-Tdc/CNTs and Ni-Tdc samples.

The microstructures of Ni-Tdc/CNT composites were analyzed by SEM and TEM measurements. As shown in Fig. 2, compared with the Ni-Tdc (Fig. S1, ESI†), upon the introduction of CNTs, the MOF nanosheets were gradually dispersed, forming a sample structure in which 2D MOF nanosheets were intertwined with 1D CNTs. It was suggested by this observation that the crystallization and growth of MOFs were induced to a certain degree by the presence of CNTs. Metal ions from the reaction system were adsorbed by the oxygen-containing functional groups on the surface of carboxylated CNTs through electrostatic interactions, thereby directing the growth of MOF nanosheets.[29] The SEM images of Ni-Tdc/CNTs-10 indicate that, with a small amount of CNTs having been introduced, insufficient crosslinking between the CNTs and the MOFs was achieved (Fig. 2a and b). When the additional amount of carboxylated CNTs added was 20 mg, a relatively loose and continuous structure was exhibited by Ni-Tdc/CNTs-20 (Fig. 2c and d), with the lateral dimensions of its continuous nanosheets exceeding those of the pristine MOFs. This structure offers ample space for the use of electrochemically active sites, which is conducive to enhancing the electrode reaction kinetics. Additionally, when a larger amount of CNTs was added to form Ni-Tdc/CNTs-30 and Ni-Tdc/CNTs-40, pronounced agglomeration was observed (Fig. 2e–h). The exposure to accessibility sites in the complex was harmful, and the mass transfer process was hindered. Therefore, when CNTs were introduced in appropriate amounts, Ni-Tdc/CNT composite structures with large lateral dimensions and staggered continuity were formed. The morphological control effect of CNTs exhibits a threshold behavior: at low concentrations, they directionally guide MOF growth, while excessive amounts lead to structural disorder due to agglomeration. The optimal ratio achieves a balance between conductive network formation and active site exposure. Further analysis of Ni-Tdc/CNTs-20 was conducted using TEM. As shown in Fig. S2(a) (ESI†), the sample structure of MOFs and CNTs can be seen in the image of Ni-Tdc/CNTs-20, and some CNTs were embedded in the MOF nanosheets, which provided an effective channel for electron transport. As shown in Fig. S2(b) (ESI†), the lattice stripe spacing of 0.34 nm in the HRTEM image of the Ni-Tdc/CNTs-20 corresponds to the (002) crystalline plane of the CNTs,[30] which also proves the successful introduction of CNTs into the composite structure.

Increasing the specific surface area of a material is another key factor in enhancing its specific capacitance. As shown in Fig. 3 and Table S1 (ESI†), the specific surface areas of Ni-Tdc and Ni-Tdc/CNTs-20, obtained from N_2 adsorption–desorption isotherms were 16.41 and 35.27 $m^2\ g^{-1}$, respectively. The adsorption properties were related to the pores formed by the stacking of nanosheets, which aligned with the SEM observations (Fig. S1 and S2, ESI†). The pore volumes of Ni-Tdc and Ni-Tdc/CNTs-20 were 0.000729 and 0.004838 $cm^3\ g^{-1}$, respectively; the pore volume increased by 85%. This indicated that Ni-Tdc/CNTs-20 had a higher specific surface area and larger pore volume, which not only enhanced the distribution of effective surface charges but also increased redox-active sites and provided good ion diffusion pathways, resulting in a higher specific capacitance.

Raman testing was performed to investigate the structural and compositional results for Ni-Tdc/CNTs-20 and Ni-Tdc samples. As shown in Fig. S3 (ESI)†, the characteristic peaks at 1465 cm^{-1} and 1592 cm^{-1} were identified as belonging to the C–C stretching vibration of the thiophene ring and the complex

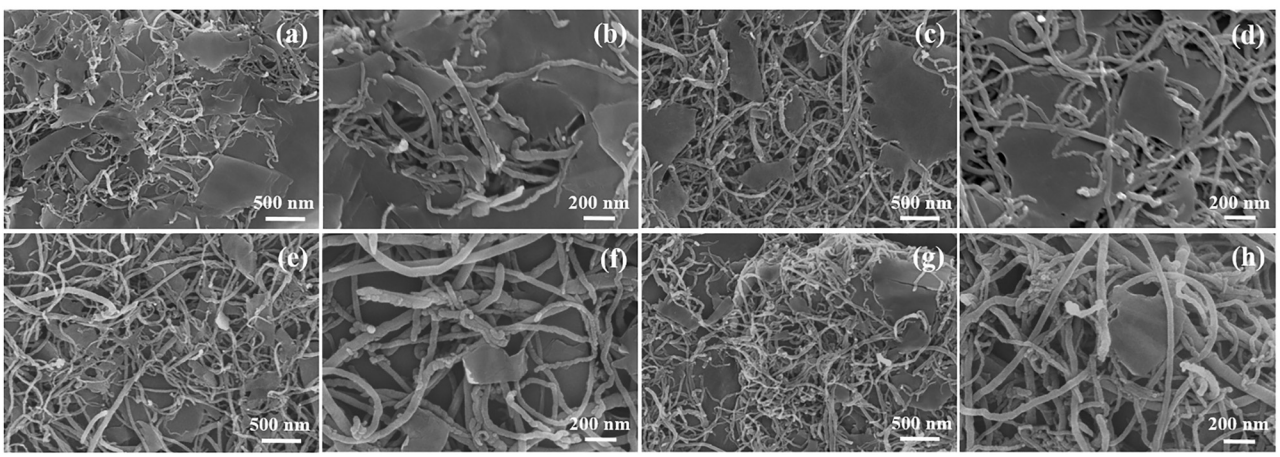

Fig. 2 SEM images of Ni-Tdc/CNT composites with different magnification: (a) and (b) Ni-Tdc/CNTs-10; (c) and (d) Ni-Tdc/CNTs-20; (e) and (f) Ni-Tdc/CNTs-30; (g) and (h) Ni-Tdc/CNTs-40.

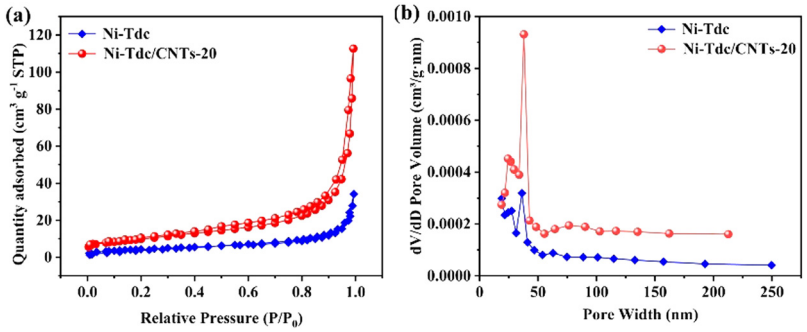

Fig. 3 (a) N_2 adsorption–desorption isotherms and (b) pore size distribution of Ni-Tdc and Ni-Tdc/CNTs-20.

vibration of the carboxylic acid group, respectively, in the Ni-Tdc spectrum, and the Raman characteristic peak at 806 cm^{-1} was corresponding to the C–S–C stretching vibration.[31–33] In the spectrum of Ni-Tdc/CNTs-20, characteristic Raman peaks with reduced intensity were also observed at the same position. Additionally, characteristic peaks at 1339 cm^{-1} and 1569 cm^{-1}, which belong to the D and G peaks of carbon, were also observed in the Raman spectra of Ni-Tdc/CNTs-20.[26,34] Raman spectroscopy analysis showed that the sample materials had been successfully introduced with CNTs while maintaining the original MOFs structure. XPS testing was performed to investigate the elemental composition and oxidation states of Ni-Tdc and Ni-Tdc/CNTs-20. The XPS test results for Ni-Tdc are shown in Fig. S4 (ESI†). The survey spectrum demonstrated that Ni, O, C, and S elements were present in the Ni-Tdc/CNTs-20 (Fig. 4a). The high-resolution XPS spectrum of Ni 2p, as shown in Fig. 4(b), displayed two resolved peaks at 873.6 eV and 855.8 eV. These peaks are attributed to the Ni 2p1/2 and Ni 2p3/2 orbitals of Ni^{2+}, respectively. Furthermore, the spectrum is accompanied by two distinct satellite peaks (designated as "Sat") at 861.1 eV and 879.5 eV.[35] This observation indicates that Ni^{2+} was successfully incorporated into the coordination within the MOF structure. In the C 1s spectrum of Ni-Tdc/CNTs-20 (Fig. 4c), the peaks observed at 284.4 eV, 284.9 eV, and 287.8 eV were attributed to C=C, C–C, and O–C=O bonds, respectively. Furthermore, the peak at 291.0 eV was identified as belonging to the π–π* transition of CNTs.[36] The high-resolution O 1s spectrum (Fig. 4d) indicates that a composite material comprising CNTs and MOFs was successfully formed. Two distinct features were observed in this spectrum at binding energies of 531.0 eV and 532.5 eV. These peaks were, respectively, attributed to Ni–O and O–C=O bonds, further confirming that coordination had occurred between the metal centers and the carboxyl groups within the thiophene ligands.[37]

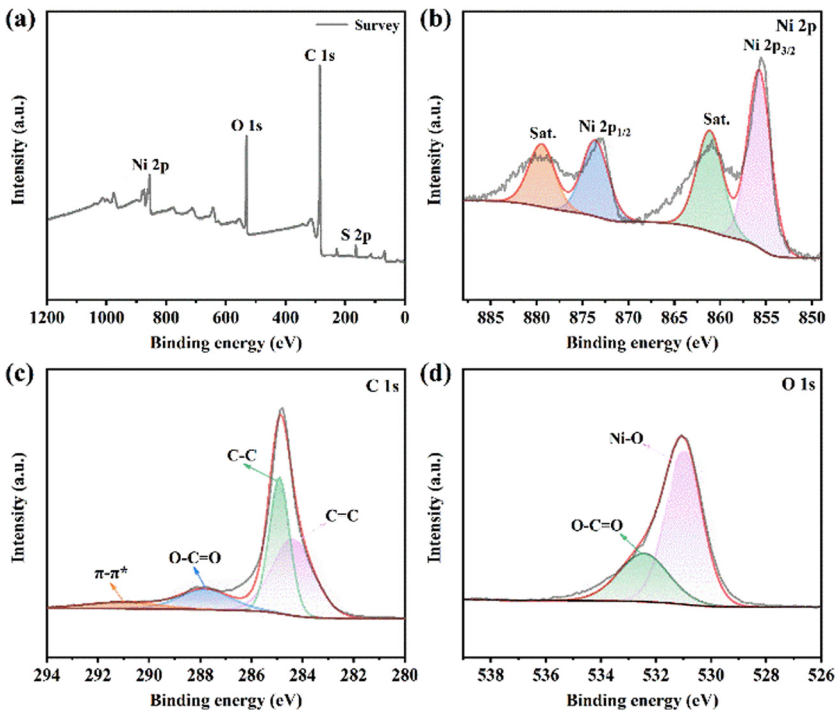

Fig. 4 XPS spectra of Ni-Tdc/CNTs-20: (a) survey spectrum and (b) Ni 2p, (c) C 1s, and (d) O 1s core spectra.

3.2. Electrochemical characterization

The electrochemical performance of the samples was explored *via* CV, Galvanostatic Charge–Discharge (GCD), and EIS measurements in a three-electrode system with a 1 M KOH electrolyte solution by an electrochemical workstation. The mass loadings of the active materials for various electrodes used in the electrochemical measurements are summarized in Table S2 (ESI†). Fig. 5a shows the comparison of the CV curves between Ni-Tdc and Ni-Tdc/CNT composites with different amounts of introduced CNTs; the voltage window of the CV curve is 0–0.6 V (*vs.* Hg/HgO). The CV curves of all electrodes exhibited a series of redox peaks at 10 mV s^{-1}, indicating that the composites remained battery-type materials even after the inclusion of CNTs. This pair of redox peaks arises from the interaction between OH^- in the electrolyte and Ni^{2+}/Ni^{3+} in the electrode material, and its specific reversible transformation can be described using the following equation:

$$\text{Ni(II)–MOF} + OH^- \rightleftharpoons \text{Ni(III)–(OH)MOF} + e^-$$

As shown in Fig. 5a, the sample with the highest energy storage capacity is Ni-Tdc/CNTs-20, exhibiting the biggest CV curve area with 20 mg of additional CNTs.

To further ascertain the specific capacity values of various electrode materials, GCD tests were conducted at a potential range of 0–0.5 V and a current density of 1 A g^{-1}. As shown in Fig. 5b, the GCD curves of all electrode materials exhibited a relatively flat charge and discharge platform, consistent with the redox peak of the CV curve, further confirming that the electrode measured was a battery-type material. A comparison of charging and discharging times revealed that the Ni-Tdc/CNTs-20 electrode exhibited longer charging times than the Ni-Tdc electrode and other Ni-Tdc/CNT electrodes, indicating that the introduction of CNTs improved the capacity performance of Ni-Tdc and that a 20 mg introduction of CNTs enhanced the electrode's capacitance. The results indicated that the introduction of CNTs improved the capacity performance of Ni-Tdc, and the electrode capacity was the highest when 20 mg of CNTs were introduced. This finding was in alignment with the analysis results obtained from the CV curves. The introduction of CNTs increased in capacity for Ni-Tdc/CNTs-20. This improvement was due to two main factors: first, the interlacing of CNTs with MOF nanosheets provided

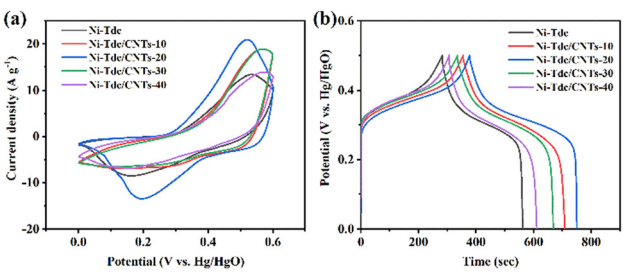

Fig. 5 Electrochemical performances of Ni-Tdc and Ni-Tdc/CNTs with varying amounts o CNTs: (a) CV curves at 10 mV s^{-1} and (b) GCD curves at 1 A g^{-1}.

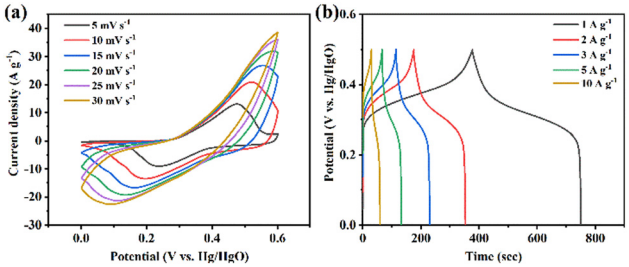

Fig. 6 Electrochemical performances of Ni-Tdc/CNTs-20: (a) CV curves at different scan rates and (b) GCD curves at different current densities.

effective electron-transmission channels and enhanced the conductivity of the composites; second, the presence of CNTs affected the crystallisation and growth of MOFs, resulting in nanosheets with larger lateral dimensions that exposed more active sites, shortened the mass transfer path of electrolyte ions, and improved the electrode reaction efficiency.

To further investigate the electrochemical behaviors of the Ni-Tdc/CNTs-20, CV tests at various scan rates and GCD tests under different current densities were conducted to investigate the material. Fig. 6a shows the CV curve of Ni-Tdc/CNTs-20 in the range of 5 to 30 mV s^{-1}. As the sweep speed increased, the anodic oxidation peak gradually moved to a higher potential, and the cathode reduction peak moved in the opposite direction. This phenomenon can be attributed to the escalating impedance within the electrode reaction process as the scan rate progressively augments. Even at higher scan rates, the CV curve shape was well observed, indicating the excellent magnification performance of Ni-Tdc/CNTs-20. Fig. 6b shows the GCD curves of Ni-Tdc/CNTs-20 in the range of 1–10 A g^{-1}, the GCD curves show a gentle charging/discharging plateau at different current densities, which further indicates the characteristics of the battery-type materials. The mass-specific capacity of the sample was calculated from the discharge time using eqn (1). At current densities of 1, 2, 3, 5, and 10 A g^{-1}, respectively, the gravimetric specific capacities of Ni-Tdc/CNTs-20 were determined to be 373.1 C g^{-1} (757.8 F g^{-1}), 354.8 C g^{-1} (712.3 F g^{-1}), 346.2 C g^{-1} (692.1 F g^{-1}), 332 C g^{-1} (668.5 F g^{-1}), and 296.3 C g^{-1} (596.7 F g^{-1}). Even at a high current density of 10 A g^{-1}, the gravimetric specific capacity of Ni-Tdc/CNTs-20 retains an impressive 79.4% of its capacity. Compared to the currently reported MOFs-based electrode materials, Ni-Tdc/CNTs-20 exhibits a comparable, slightly better specific capacity and rate performance (Table S3, ESI†).

To systematically investigate the impact of varying CNT concentrations on the energy storage capabilities of composites, GCD curves were acquired for Ni-Tdc, Ni-Tdc/CNTs-10, Ni-Tdc/CNTs-30, Ni-Tdc/CNTs-40, and Ni-Tdc/CNTs-20 within a current density range of 1–10 A g^{-1}. As shown in Fig. S4 (ESI†) and Fig. 6(b), 7(a–c), the GCD curves of all four sample electrodes showed similar shapes, suggesting that the Ni-Tdc/CNT electrodes have the same capacity storage mechanism. The mass-specific capacities, determined from GCD measurements at 1 A g^{-1}, exhibited values of 352.8 C g^{-1} (705.4 F g^{-1}), 373.1 C g^{-1}

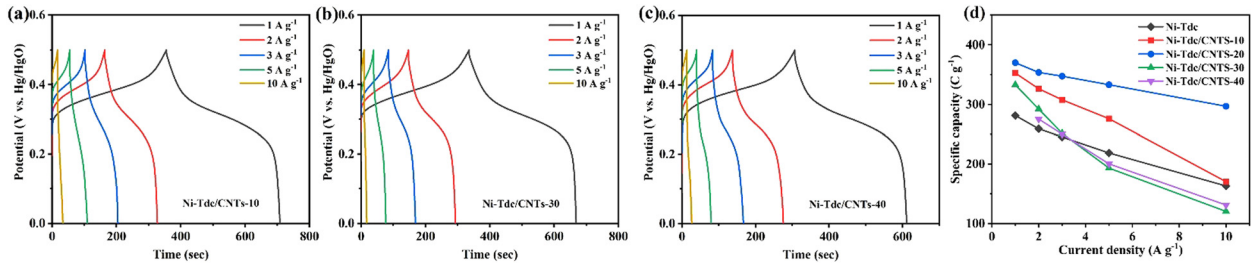

Fig. 7 GCD curves of different Ni-Tdc/CNT electrodes at different current densities: (a) Ni-Tdc/CNTs-10; (b) Ni-Tdc/CNTs-30; and (c) Ni-Tdc/CNTs-40. (d) Rate performance of Ni-Tdc and four Ni-Tdc/CNT electrodes.

(757.8 F g^{-1}), 332.9 C g^{-1} (613.9 F g^{-1}), and 304.5 C g^{-1} (609.4 F g^{-1}) for the sample electrodes containing 10, 20, 30, and 40 mg of CNTs, respectively, superior to the 279.4 C g^{-1} (561 F g^{-1}) of Ni-Tdc under the same conditions. The capacity retention of Ni-Tdc, Ni-Tdc/CNTs-10, Ni-Tdc/CNTs-20, Ni-Tdc/CNTs-30, and Ni-Tdc/CNTs-40 electrodes was 54.7, 47.2, 79.4, 35.5, and 43.2%, respectively, when the current density was increased to 10 A g^{-1}. Compared with the specific capacity of each electrode at different current densities (Fig. 7d), the energy storage performance of MOF sample electrodes with the introduction of an appropriate amount of CNTs (20 mg) was maximally enhanced, which was mainly due to the improvement of the electron transport channels and redox activity of MOF materials by the appropriate amount of CNTs. The regulation of crystallisation and growth of MOFs is limited when CNTs are introduced in small amounts, and the enhancement of the electrical conductivity is not significant. In another instance, excessive incorporation of CNTs led to excessive accumulation and aggregation of MOFs and CNTs, which hindered the contact between electrolyte ions and active sites, thereby limiting the electrochemical reaction activity. In addition, this excessive incorporation may have resulted in the disruption of the conductive network architecture.

The charge transport impedance of Ni-Tdc/CNT electrode materials with different CNT introduction levels was analyzed using the EIS test. As shown in Fig. 8a, the Nyquist plot exhibited two components: a semicircular region in the high-frequency range and a sloping linear section in the low-frequency range. The intersection with the real axis (Z') corresponds to the series resistance (R_s), and the diameter of the semicircle corresponds to the charge transfer impedance (R_{ct}). The R_s values of Ni-Tdc, Ni-Tdc/CNTs-10, Ni-Tdc/CNTs-20, Ni-Tdc/CNTs-30, and Ni-Tdc/CNTs-40 were 0.93, 1.05, 0.77, 1.12, and 1.06 Ω, respectively, which indicates that the composite material has the smallest equivalent series resistance value for the introduction of 20 mg of CNTs. The Ni-Tdc/CNTs-20 electrode exhibited the smallest arc region, indicative of its minimal Rct. These observations can be attributed to the enhancement in conductivity facilitated by the incorporation of an appropriate amount of CNTs, coupled with the growth of large-sized nanosheets. The construction of conductive networks plays a pivotal role in enhancing electrode performance. Shoeb *et al.*[38] proved that the synergistic interaction between MXene and $NiCo_3S_4$ reduced the charge-transfer resistance (R_{ct}) to 10.05 Ω, while optimized mass loading (2.5 mg cm^{-2}) achieved the maximum specific capacitance. Furthermore, the highest slope of the straight line in the low-frequency region was exhibited by Ni-Tdc/CNTs-20, indicating that this electrode possessed a faster diffusion rate of electrolyte ions. The long-cycle test results of the Ni-Tdc/CNTs-20 are presented in Fig. 8b. At a current density of 10 A g^{-1}, the Ni-Tdc/CNTs-20 exhibited a capacity retention rate of 67.3% after undergoing 3000 charge–discharge cycles, demonstrating its better cycling performance.

To elucidate the electrochemical energy storage mechanism of Ni-Tdc/CNTs-20, the contributions of diffusion-controlled and capacitance-controlled currents were examined *via* CV curves. The current response can be described according to eqn (3) and (4), A "*b*" value of 1 indicates a process unaffected by diffusion, which is attributed to surface redox reactions, while a "*b*" value of 0.5 suggests a diffusion-controlled faradaic process. The values between 0.5 and 1 imply the simultaneous

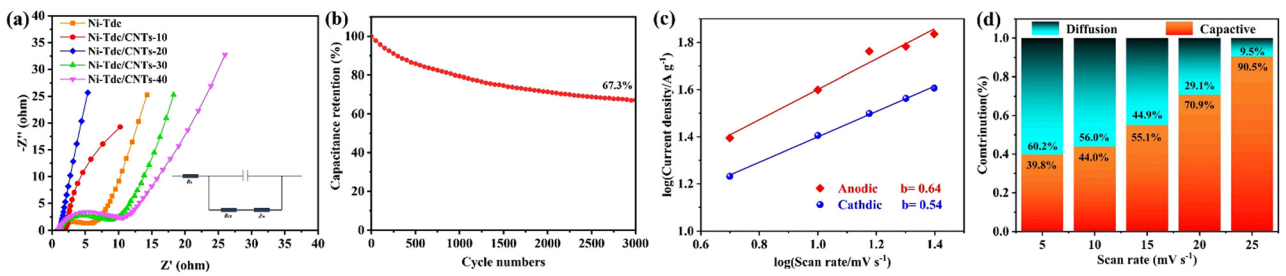

Fig. 8 (a) Nyquist plots of Ni-Tdc and four Ni-Tdc/CNT electrode materials (inset: equivalent electrical circuit). (b) Cycling stability of Ni-Tdc/CNTs-20 at 10 A g^{-1} for 3000 cycles. (c) Determination of the *b*-value for Ni-Tdc/CNTs-20. (d) Percentage of the capacitive and diffusion contribution in charge storage at different scan rates for Ni-Tdc/CNTs-20.

occurrence of both mechanisms in charge storage.[39] As shown in Fig. S6 (ESI†), a pair of prominent redox peaks appear within the potential range of 0–0.6 V (*vs.* Hg/HgO), indicating a reversible electrode reaction and suggesting that energy storage occurs *via* a faradaic process. As shown in Fig. 8c, the "*b*" values are 0.64 (peak 1) and 0.54 (peak 2), suggesting that the process is predominantly diffusion-controlled. At a scan rate of 5 mV s^{-1}, the capacitive and diffusive contributions for the Ni-Tdc/CNTs-20 electrode are 39.8% and 60.2%, respectively (Fig. 8d), indicating that diffusion-controlled faradaic behavior dominates at lower scan rates. The scan rate increased with the capacitive contribution reaching 90.5% at 25 mV s^{-1}, which indicates rapid electrochemical kinetics at higher scan rates.

To investigate the performance of Ni-Tdc/CNTs-20 electrode in real supercapacitor devices, Ni-Tdc/CNTs-20//AC asymmetric devices were assembled using Ni-Tdc/CNTs-20 as the positive electrode and AC as the negative electrode. Fig. 9(a) shows the voltage window of the CV curve of AC and Ni-Tdc/CNTs-20 at 5 mV s^{-1}, from −1 to 0 V, and from 0 to 0.6 V, respectively. CV testing of the Ni-Tdc/CNTs-20//AC devices was conducted within a voltage window ranging from 0 to 1.6 V. The CV curve exhibited the characteristics of both double-layer capacitance and battery capacitors (Fig. 9b), and it maintained a similar shape across the scan rate range of 10–100 mV s^{-1}, without any notable distortion. These results indicate that the device has a relatively superior rate capability. Further evaluation of the device's capacitive performance was conducted through GCD testing within a voltage window of 0–1.6 V (Fig. 9c). The excellent symmetry observed in the GCD curves aligns well with the outcomes of CV analysis. Based on the discharge time obtained from the GCD curves and eqn (2), the mass-specific capacitances of the Ni-Tdc/CNTs-20//AC device were determined to be 126.9, 108.7, 97.5, 84.4, and 62.5 F g^{-1} at current densities of 1, 2, 3, 5, and 10 A g^{-1}, respectively. At a current density of 1 A g^{-1}, the Ni-Tdc/CNTs-20//AC device achieved an energy density of 45 W h kg^{-1} and a power density of 798 W kg^{-1}, as calculated using eqn (6) and (7). Notably, even at a higher power density of 8000 W kg^{-1}, the device retained an energy density of 22.2 W h kg^{-1}. Fig. 9d shows the results of the long-cycle stability test conducted on the Ni-Tdc/CNTs-20//AC device, revealing that the specific capacitance remained at 74.1% of its initial value after 5000 consecutive galvanostatic charge–discharge cycles. The robust cycling stability of the composite material was attributed to the incorporation of CNTs, which mitigated volume changes during charge–discharge processes and thereby enhanced material stability. Consequently, the strategy of combining CNTs with MOF materials effectively enhanced the electrochemical performance of the resulting material.

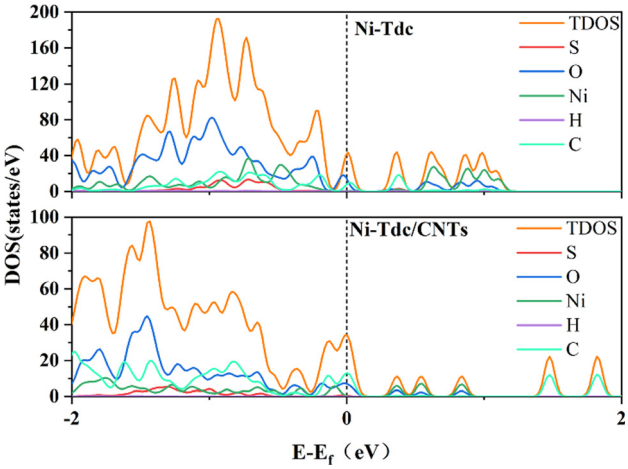

Fig. 10 Total and atom projected TDOS of Ni-Tdc and Ni-Tdc/CNTs. The vertical black dashed line denotes the Fermi level.

3.3. Density functional theory analysis

To analyze the impact of varying Ni/Co atomic ratios on the electronic structure, DFT calculations were performed for four different states. Based on the aforementioned *in situ* and *ex situ* characterization results, atomic structural models for Ni-Tdc and Ni-Tdc/CNTs were constructed (Fig. S7, ESI†). The carbon nanotube support can be approximated as a graphene sheet, simplifying the model complexity and reducing the computational burden, thus providing a novel approach for studying carbon nanotube supports.[40] For computational convenience, graphene was used to represent carbon nanotubes in the modeling. The differential local charge density and density of states (DOS) were employed to elucidate the electronic interactions within Ni-Tdc/CNTs. As shown in Fig. 10, the enhanced DOS near the Fermi level in Ni-Tdc/CNTs was primarily attributed to electron injection from the C in the CNTs. This electronic structure effectively accelerates electron transfer, thereby improving the conductivity of the electrode. Furthermore, the charge

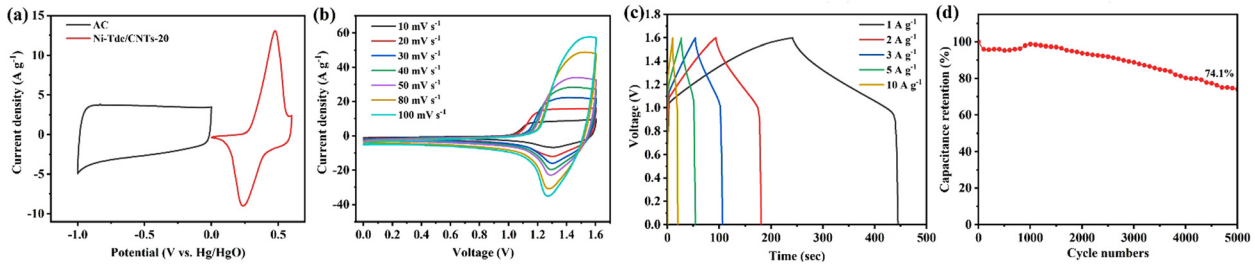

Fig. 9 (a) CV curves of Ni-Tdc/CNTs-20 and AC at 5 mV s^{-1}. (b) CV profiles of Ni-Tdc/CNTs-20//AC device at various sweep rates. (c) GCD plots of Ni-Tdc/CNTs-20//AC device at different current densities. (d) Cycle stability of Ni-Tdc/CNTs-20//AC device at 10 A g^{-1}.

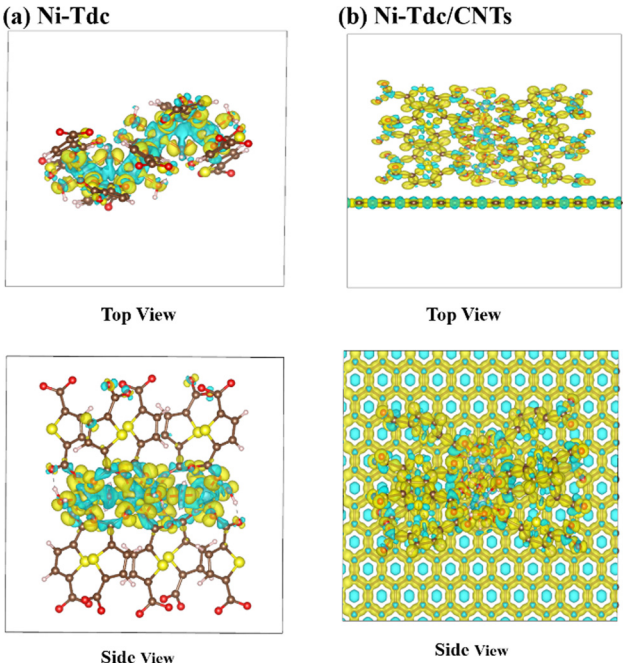

Fig. 11 Charge density difference of (a) Ni-Tdc; (b) Ni-Tdc/CNTs. The yellow region represents electron accumulation and cyan region represents electron depletion.

transfer in the most stable geometric structures of Ni-Tdc and Ni-Tdc/CNTs was analyzed using the Bader charge method.[41] The calculated net charge differences for Ni-Tdc and Ni-Tdc/CNTs were −0.6 eV, respectively, indicating charge transfer from CNTs to Ni-Tdc, represented by this negative charge. As illustrated in Fig. 11, compared with Ni-Tdc, Ni-Tdc/CNTs showed greater electron accumulation (yellow regions), indicating charge redistribution and enhanced proton interactions. The CNTs act as electron donors, enhancing the electronic conductivity of the composite and facilitating efficient charge transport at the electrode–electrolyte interface. This charge transfer contributes to the improved electrochemical performance of the Ni-Tdc/CNTs composite by increasing the number of charge carriers available for redox reactions and improving the overall conductivity of the material.

4. Conclusions

In conclusion, Ni-Tdc/CNT composites with large lateral dimensions and staggered continuity were successfully synthesized using CNTs and MOFs. The introduced CNTs promoted electron transport within the electrode materials, while the nanostructures provided ample space for electrolyte ions to contact the active sites, thereby effectively enhancing the use of redox-active sites. Benefiting from the nanocomposite structure, the synthesized Ni-Tdc/CNTs-20 electrode exhibited a high specific capacity of 373.1 C g^{-1} at 1 A g^{-1} and maintained a high rate capacity retention of 79.4% at 10 A g^{-1}. In addition, an asymmetric supercapacitor device (Ni-Tdc/CNTs-20//AC) was assembled using Ni-Tdc/CNTs-20 and AC as the positive and negative electrodes, respectively, achieving a maximum energy density of 45 W h kg^{-1} at a power density of 798 W kg^{-1}. This work explores the potential of integrating 2D MOFs and CNTs.

Data availability

All data supporting the findings of this study are included in the article and its ESI.†

Conflicts of interest

There are no conflicts to declare.

Acknowledgements

We gratefully acknowledge the financial support from the Guangdong Basic and Applied Basic Research Foundation (2024A1515030172), the College Students Innovative Entrepreneurial Training Plan Program (202411847006), and Guangxi Key Laboratory of Green Chemical Materials and Safety Technology, College of Petroleum and Chemical Engineering, Beibu Gulf University (2023SYSZZ07).

References

1 T. Guo, D. Zhou, L. Pang, S. Sun, T. Zhou and J. Su, *Small*, 2022, **18**, 2106360.
2 S. J. Shin, J. W. Gittins, C. J. Balhatchet, A. Walsh and A. C. Forse, *Adv. Funct. Mater.*, 2024, **34**, 2308497.
3 S. Najib and E. Erdem, *Nanoscale Adv.*, 2019, **1**, 2817–2827.
4 P. A. Shinde, Y. Seo, S. Lee, H. Kim, Q. N. Pham, Y. Won and S. C. Jun, *Chem. Eng. J.*, 2020, **387**, 122982.
5 S. Sanati, R. Abazari, J. Albero, A. Morsali, H. García, Z. B. Liang and R. Q. Zou, *Angew. Chem., Int. Ed.*, 2021, **60**, 11048–11067.
6 G. Q. Song, C. D. Li, T. Wang, K. H. Lim, F. Y. Hu, S. W. Cheng, E. Hondo, S. M. Liu and S. Kawi, *Small*, 2024, **20**, 2305517.
7 P. Naskar, A. Maiti, P. Chakraborty, D. Kundu, B. Biswas and A. Banerjee, *J. Mater. Chem. A*, 2021, **9**, 1970–2017.
8 J. Khan, A. Khan, B. Rubab, F. Jamshaid, A. A. Al-Kahtani and A. Dahshan, *Appl. Mater. Today*, 2023, **34**, 101906.
9 M. Shoeb, F. Mashkoor, M. Naved Khan, B.-J. Kim and C. Jeong, *Sep. Purif. Technol.*, 2025, **354**, 128656.
10 Y. L. Shao, M. F. El-Kady, J. Y. Sun, Y. G. Li, Q. H. Zhang, M. F. Zhu, H. Z. Wang, B. Dunn and R. B. Kaner, *Chem. Rev.*, 2018, **118**, 9233–9280.
11 M. Azadfalah, A. Sedghi, H. Hosseini and H. Kashani, *J. Energy Storage*, 2021, **33**, 101925.
12 R. Bendi, V. Kumar, V. Bhavanasi, K. Parida and P. S. Lee, *Adv. Energy Mater.*, 2015, **6**, 1501833.
13 T. Wang, H. C. Chen, F. Yu, X. S. Zhao and H. X. Wang, *Energy Storage Mater.*, 2019, **16**, 545–573.
14 Y. J. Zhou, Z. M. Mao, W. Wang, Z. K. Yang and X. Liu, *ACS Appl. Mater. Interfaces*, 2016, **8**, 28904–28916.

15 B. T. Niu, X. L. Li, W. N. Xia, Y. W. Wu, S. M. Ying and H. X. Guo, *Synth. Met.*, 2022, **287**, 117073.
16 X. Y. Chu, F. L. Meng, W. Zhang, L. H. Zhang, S. Molin, P. Jasinski and W. T. Zheng, *Mater. Res. Lett.*, 2023, **11**, 446–453.
17 Y. Han, J. Zhou, L. Wang, L. Xing, Z. Xue, Y. Jiao and Y. Pang, *J. Electroanal. Chem.*, 2021, **882**, 114993.
18 H. Zhang, K. Zhao, W. Guo, K. Liang, J. Li, X. Li, Q. Deng, X. Xu, H. Chao, H. Xi and C. Duan, *Intensive Care Med.*, 2025, **3**, 109–121.
19 K. Liang, W. Guo, L. Li, H. Cai, H. Zhang, J. Li, F. Xu, J. Yan, D. Lv, H. Xi and C. Duan, *Nano Mater. Sci.*, 2024, **6**, 467–474.
20 Y. X. Liu, Y. Z. Wang, H. Q. Wang, P. H. Zhao, H. Hou and L. Guo, *Appl. Surf. Sci.*, 2019, **492**, 455–463.
21 D. D. Chronopoulos, H. Saini, I. Tantis, R. Zboril, K. Jayaramulu and M. Otyepka, *Small*, 2022, **18**, 2104628.
22 X. J. Li, J. F. Ping and Y. B. Ying, *TrAC-Trend Anal. Chem.*, 2019, **113**, 1–12.
23 M. Shoeb, F. Mashkoor, H. Jeong, M. N. Khan and C. Jeong, *Small*, 2025, **21**, e2408283.
24 F. T. Ran, X. Q. Xu, D. Pan, Y. Y. Liu, Y. P. Bai and L. Shao, *Nano-Micro Lett.*, 2020, **12**, 46.
25 A. Demessence, A. Mesbah, M. François, G. Rogez and P. Rabu, *Eur. J. Inorg. Chem.*, 2009, 3713–3720.
26 P. Wen, P. W. Gong, J. F. Sun, J. Q. Wang and S. R. Yang, *J. Mater. Chem. A*, 2015, **3**, 13874–13883.
27 X. Hang, J. Zhao, Y. Xue, R. Yang and H. Pang, *J. Colloid Interface Sci.*, 2022, **628**, 389–396.
28 S. Y. Song, X. Y. Ma, B. Y. Zhang, W. Y. Li, Y. S. Feng and C. L. Tan, *J. Energy Storage*, 2022, **47**, 103627.
29 K.-J. Tsai, C.-S. Ni, H.-Y. Chen and J.-H. Huang, *J. Power Sources*, 2020, **454**, 227912.
30 J. Deng, C. Wang, G. Z. Guan, H. Wu, H. Sun, L. B. Qiu, P. N. Chen, Z. Y. Pan, H. Sun, B. Zhang, R. C. Che and H. S. Peng, *ACS Nano*, 2017, **11**, 8464–8470.
31 S. S. Margreat, S. Ramalingam, S. Sebastian, S. Xavier, S. Periandy, J. C. Daniel and M. M. Julie, *J. Mol. Struct.*, 2020, **1200**, 127099.
32 L. Brambilla, J. S. Kim, B. J. Kim, V. Hernandez, J. T. L. Navarrete and G. Zerbi, *J. Mol. Struct.*, 2020, **1221**, 128882.
33 M. Salmanion and M. M. Najafpour, *Int. J. Hydrogen Energy*, 2021, **46**, 19245–19253.
34 L. Yaqoob, T. Noor, N. Iqbal, H. Nasir, N. Zaman and K. Talha, *J. Alloys Compd.*, 2021, **850**, 156583.
35 S. W. Gao, Y. W. Sui, F. X. Wei, J. Q. Qi, Q. K. Meng, Y. J. Ren and Y. Z. He, *J. Colloid Interface Sci.*, 2018, **531**, 83–90.
36 X. N. Chen, X. H. Wang and D. Fang, *Fullerenes, Nanotubes Carbon Nanostruct.*, 2020, **28**, 1048–1058.
37 W. Zhao, Y. W. Zheng, L. Cui, D. D. Jia, D. Wei, R. K. Zheng, C. Barrow, W. R. Yang and J. Q. Liu, *Chem. Eng. J.*, 2019, **371**, 461–469.
38 M. Shoeb, F. Mashkoor, J. A. Khan, M. N. Khan, M. A. Gondal and C. Jeong, *J. Energy Storage*, 2024, **97**, 112654.
39 M. Isacfranklin, R. Yuvakkumar, G. Ravi, D. Velauthapillai, M. Pannipara and A. G. Al-Sehemi, *Nanoscale Adv.*, 2021, **3**, 486–498.
40 Y. Zhu, S. Zhi and B. Wan, *Electrochim. Acta*, 2025, **511**, 145384.
41 G. Henkelman, A. Arnaldsson and H. Jónsson, *Comput. Mater. Sci.*, 2006, **36**, 354–360.

